Proceedings of the 21st ICSMGE, Vienna, Austria, 14 – 19 June 2026. Pistrol, Adam & Schweiger (eds.)
Published by: ÖGG, Austrian Society for Geomechanics, Salzburg, Austria, ISBN 978-3-9503898-4-5
https://doi.org/10.53243/ICSMGE2026-2314

Full-field measurement of three-phase microstructures in partially saturated triaxial specimen using SPring-8

Ryunosuke Kido
Hiroshima University, Department of Civil and Environmental Engineering, Japan, rkido@hiroshima-u.ac.jp

Yosuke Higo
Kyoto University, Department of Civil and Earth Resources Engineering, Japan

ABSTRACT: Partially saturated sand exhibits a more brittle failure mode with distinct shear bands compared to fully saturated and dry sand. Previous studies using X-ray micro-computed tomography (CT) during triaxial compression tests have revealed variations in porosity and degree of saturation within shear bands in partially saturated sand. However, these observations were limited to a small localized region where shear bands were likely to develop. This study aims to elucidate the development of shear bands and the resulting changes in density and degree of saturation distribution within the specimen. For this purpose, the world's largest third-generation synchrotron radiation facility, SPring-8, was used to perform triaxial compression tests on a partially saturated specimen. Digital image correlation was applied to compute shear-strain fields, while segmentation of CT images enabled calculation of void ratio (porosity) and degree of saturation. Local porosity and degree of saturation were quantified by extracting sub-volumes from the segmented images. Variations in porosity and degree of saturation along the specimen's vertical direction under triaxial compression were then analyzed. By utilizing the high-energy X-ray CT system at SPring-8, we successfully captured high-resolution images of the three-phase microstructural changes (soil particles, water, and air) throughout an unsaturated triaxial specimen with a diameter of 35 mm and a height of 71 mm. Image analysis revealed that, while the central region of the specimen exhibited a decrease in density and saturation, the upper and lower regions showed a slight increase in saturation without significant changes in density. Furthermore, under drained-air, undrained-water conditions, a marked decrease in density and water retention was observed within the shear band, along with the migration of pore water from within the shear band to the surrounding region, which exhibited higher water retention.

KEYWORDS: Partially saturated soil, triaxial compression test, full-field measurement

1 INTRODUCTION

Earth structures, such as road embankments and levees, usually exist above the groundwater level and are therefore in an unsaturated state. For the safe design, operation, and maintenance of these structures under natural hazards such as heavy rainfall and earthquakes, it is essential to evaluate the shear strength of unsaturated soils. The triaxial compression test is major method to evaluate shear strength of soils, and there are mainly three possible test conditions for unsaturated soils: drained conditions for both air and water (Cui and Delage, 1996; Cunningham et al., 2003); a drained condition for air and an undrained condition for water (Rahardjo et al., 2004; Thu et al., 2006); and undrained conditions for both air and water (Kimoto et al., 2011). However, the reliable strength evaluation method for unsaturated soils is not established. This is because macroscopic responses of soils, such as variations in deviator stress, pore fluid pressures (suction) and dilatancy, have been investigated through the triaxial compression tests, while the specific mechanism of the macroscopic responses has not been sufficiently understood. To address this issue, it is essential to clarify the microscopic characteristics of partially saturated soils that govern their macroscopic responses.

Our research group has applied X-ray micro-computed tomography (micro-CT) to triaxial compression tests and has revealed the following: (1) a partially saturated sand show a brittle failure mode with a clear shear band, more clearly than dry or fully saturated sand (Higo et al., 2011); and (2) during shear band development, the number of liquid bridges and the curvature of air-water interfaces change, which influences the deviatoric stress (Kido and Higo, 2020). However, in our previous studies, the region observable with high-resolution CT, was limited to a part of the entire specimen where was assumed to include the shear band. It is considered that microstructural changes within the shear band significantly affect the macroscopic behavior, but detailed investigations into the changes in water retention properties inside and outside the shear band have not yet been conducted. Although some studies have visualized pore water distribution throughout a partially saturated sand specimen (Wang et al., 2019), the sample sizes were extremely small (about 10 mm in diameter) to fit within the CT scanning area, resulting in very low deviatoric stresses (on the order of a few kPa). Therefore, revealing the spatial variation in water retention between the shear band and surrounding areas in a full-size unsaturated triaxial specimen would be both academically novel and practically meaningful for improving strength evaluation methods of unsaturated soils.

In this study, we conduct full-field measurements of the entire unsaturated triaxial specimen at the particle scale using a high-energy X-ray CT scanner at the large synchrotron radiation facility SPring-8. Through CT image analysis, we aim to clarify the development of shear bands and the associated changes in the internal distribution of density and degree of saturation within the specimen.

2 METHODS

2.1 *Triaxial compression tests*

Figure 1 presents a schematic illustration of the triaxial test apparatus. A transparent acrylic triaxial cell with a pressure resistance of 1 MPa was used to allow sufficient X-ray transmission while applying confining pressure to the specimen and enabling reaction force measurements during triaxial compression. The test specimen was prepared using silica sand No. 5, which has a mean particle diameter D_{50} of 456 μm (Kido and Higo, 2020). A triaxial specimen was prepared using the water pluviation method, in which the silica sand was poured into a mold filled with water. To obtain a dense sand specimen with a target relative density D_r of 90%, vibration was applied to the mold.

Following specimen preparation, a confining pressure of 50 kPa was applied. Subsequently, suction was induced by lowering the water level in a double-tube burette connected to the bottom of the specimen below the specimen's top surface, thereby promoting desaturation. A ceramic disk with an air

entry value (AEV) of 50 kPa, sufficiently higher than the water retention capacity of the silica sand, was used to ensure appropriate suction control. Throughout the desaturation process and the subsequent triaxial compression test, the top of the specimen was exposed to atmospheric pressure with a relative humidity above 99% to prevent drying. The amount of water drained was monitored until equilibrium was reached.

After desaturation, shearing was performed under a condition where air was allowed to drain while water was undrained—hereinafter referred to as the **UW test**—at a strain rate of 0.1%/min. Axial load, axial displacement, and lateral pressure were recorded. The specimen had a diameter of 35 mm, a height of 71 mm, an initial degree of saturation of 53.42%, and an initial relative density of 82.27%.

2.2 *X-ray CT observation*

The experiments were conducted using beamline BL28B2 at the large synchrotron radiation facility SPring-8. At SPring-8, electrons emitted from the SACLA electron gun are accelerated up to 8 GeV by a linear accelerator and booster synchrotron, and then injected into a storage ring with a circumference of 1,436 meters. As the electrons circulate within the storage ring, synchrotron radiation is generated by bending magnets and insertion devices. Over time, electron losses due to scattering and other effects cause a reduction in the ring current, resulting in a shortened beam lifetime. To counteract this, SPring-8 employs a top-up injection method; that is, electrons are periodically replenished to maintain a constant ring current of up to 100 mA during normal operation, thereby stabilizing the X-ray beam intensity. The minimum configurable voxel size is 1.6 μm (Hoshino and Uesugi, 2023).

Beamline BL28B2 provides access to white synchrotron X-rays and enables high-energy X-ray imaging with a central energy of 200 keV and a spectral width of approximately 100 keV (Hoshino et al., 2017). The X-ray imaging system (Hoshino et al., 2020) consists of a 500 μm-thick LuAG ceramic plate used as a scintillator to convert incident X-rays into visible light, an optical lens system to project the image onto the image sensor, and a CMOS digital camera for image acquisition. Figure 2 shows the setup of the triaxial compression testing apparatus mounted on the CT worktable. During CT scanning, triaxial loading was temporarily paused. At BL28B2, each scan captured an area measuring 49 mm in width and 1.7 mm in height. To achieve full-field particle-scale imaging of the specimen, the worktable was incrementally raised after each scan. A total of 52 scans were performed, with a vertical step size of 1.42 mm per scan.

The authors also utilized a microfocus X-ray CT apparatus, KYOTO-GEOμXCT (TOSCANER-32250μhdk) (Kido et al., 2020). In one of our previous studies (Kido and Higo, 2020), variations in the microscopic characteristics of pore water associated with the development of shear bands in partially saturated sand were investigated. However, only a limited region where shear bands were expected to form could be visualized, as the cross-sectional images consisted of 1024 × 1024 voxels with a voxel size of 12 μm³, as shown in Figure 3. In contrast, the cross-sectional images obtained using beamline BL28B2 at SPring-8 consist of 4096 × 4096 voxels while maintaining the same voxel size of 12 μm³. This enables high-resolution observation of microstructural changes across the entire specimen, including the identification of individual particles and water retention states.

2.3 *Image analysis*

Displacement inside the specimen during shearing was calculated at regularly spaced reference points in both horizontal and vertical directions using a digital image correlation (DIC) (Higo et al., 2013) with sub-voxel refinement (Kido, 2019). Based on these displacements, the strain field was computed using the B-matrix from 8-node isoparametric elements in the finite element method. The second invariant of the deviatoric strain tensor was then obtained and used as the shear strain.

Segmentation was applied to the CT images to identify soil particle phase, pore water phase and pore air phase (Kido et al., 2020). Subsequently. small sub-volumes, namely, cubic subsets (Higo and Kido, 2024), were extracted from the segmented images, and their local void ratios and degrees of saturation were calculated, as described in Figure 4. A sensitivity analysis was performed in advance to determine an appropriate subset size that could capture local variations in porosity and saturation (Higo et al., 2018). As a result, a cubic subset with an edge length of 41 voxels was used.

The acquired CT images included both the specimen and the membrane enclosing it. Therefore, prior to conducting image analyses as mentioned above, a preliminary image processing was performed to extract only the specimen region (Figure 5). First, a binary image of the soil particle phase was obtained using the region growing method implemented in the image analysis software VGStudioMax (Figure 5a). Next, morphological operations were applied to the binary image using Avizo software: dilation of 20 voxels, hole filling, and erosion of 20 voxels, in that order (Figures 5b and 5c). Finally, the region corresponding to the processed binary image was extracted from the original CT image to isolate only the specimen (Figure 5d).

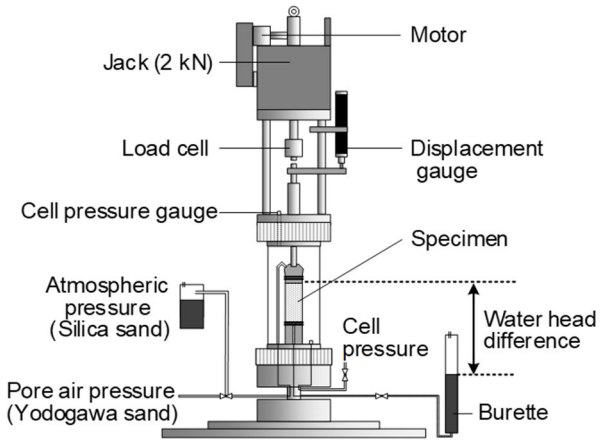

Figure 1. Specimen preparation by negative water column technique under isotropic confining pressure condition.

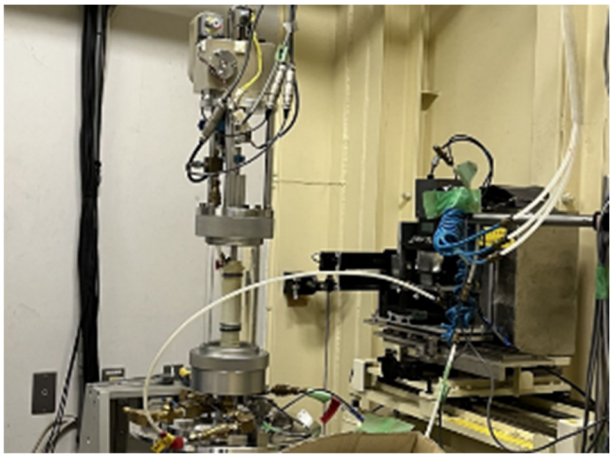

Figure 2. Triaxial test apparatus on worktable of SPring-8.

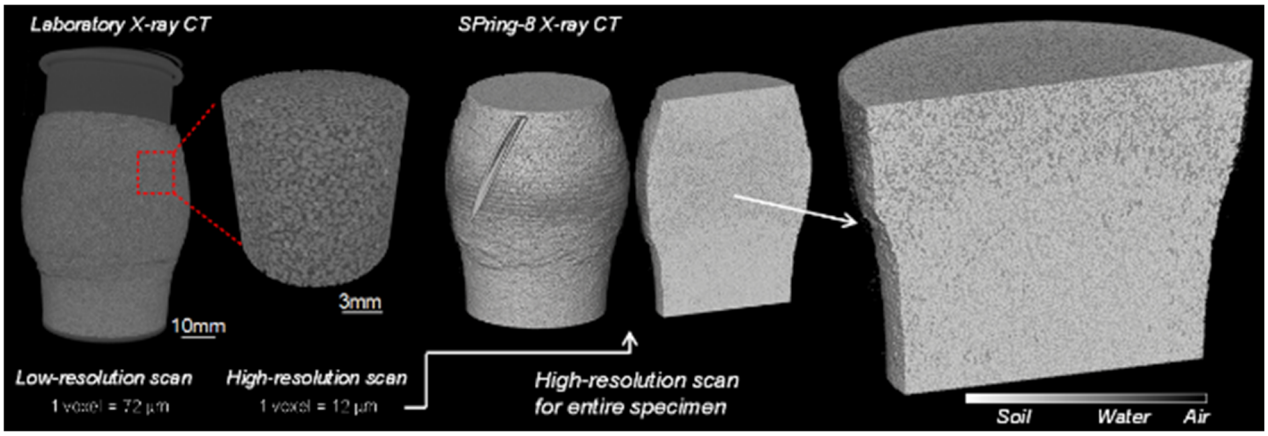

Figure 3. CT images obtained using KYOTO-GEOμXCT (Kido and Higo, 2020) and BL28B2 utilized in SPring-8.

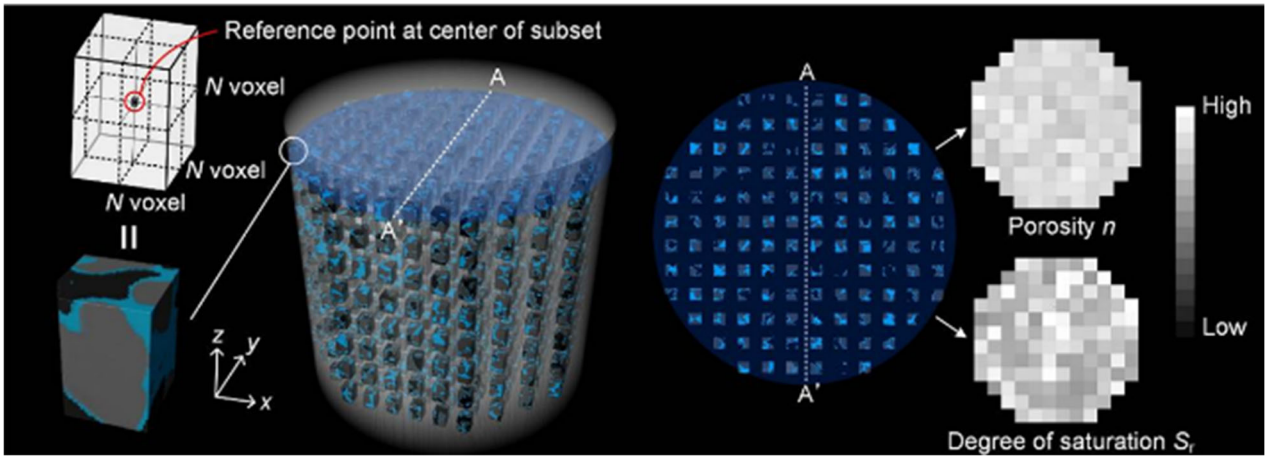

Figure 4. Method for quantifying local porosity and degree of saturation using cubic subsets (partially modified from the figure in [6])

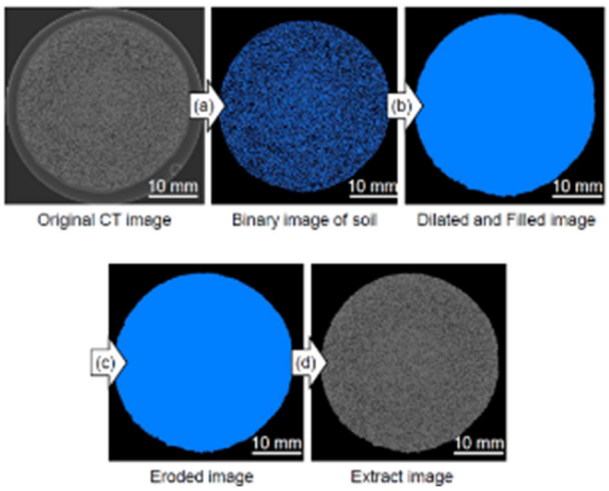

Figure 5. Image processing to extract only the specimen region from CT images.

3 RESULTS AND DISCUSSION

3.1 *Macroscopic responses*

The relationship between deviator stress and axial strain is shown in Figure 6. The deviator stress of case UW measured in a previous study (Kido and Higo, 2020) is also included in this figure. The specimens exhibit a typical behavior of densely packed sand, characterized by strain softening following the peak stress. A bit difference is observed during the softening process between the two stress curves probably due to the failure mode of the specimen since initial conditions such as density, degree of saturation, suction and so on, are not perfectly identical. Nevertheless, both results are relatively similar to each other, which confirms the repeatability of the tests

Figure 7 presents vertical cross-section images and spatial distributions of shear strain. The shear strain distribution indicates that large shear strains are concentrated along an inclined plane, while the surrounding areas show negligible shear strain. It is found from the CT images that the density changes at the middle part of the specimen, and it also locally changes in diagonal directions where the large shear strain develops. These results confirm the development of a shear band within the specimen.

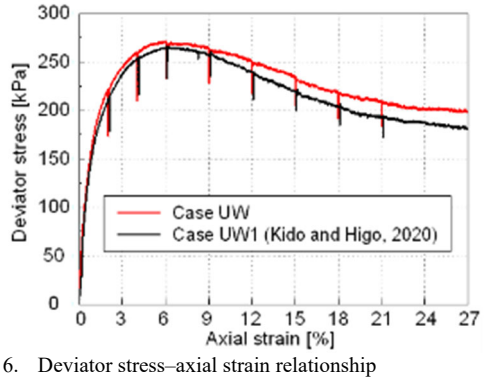

Figure 6. Deviator stress–axial strain relationship

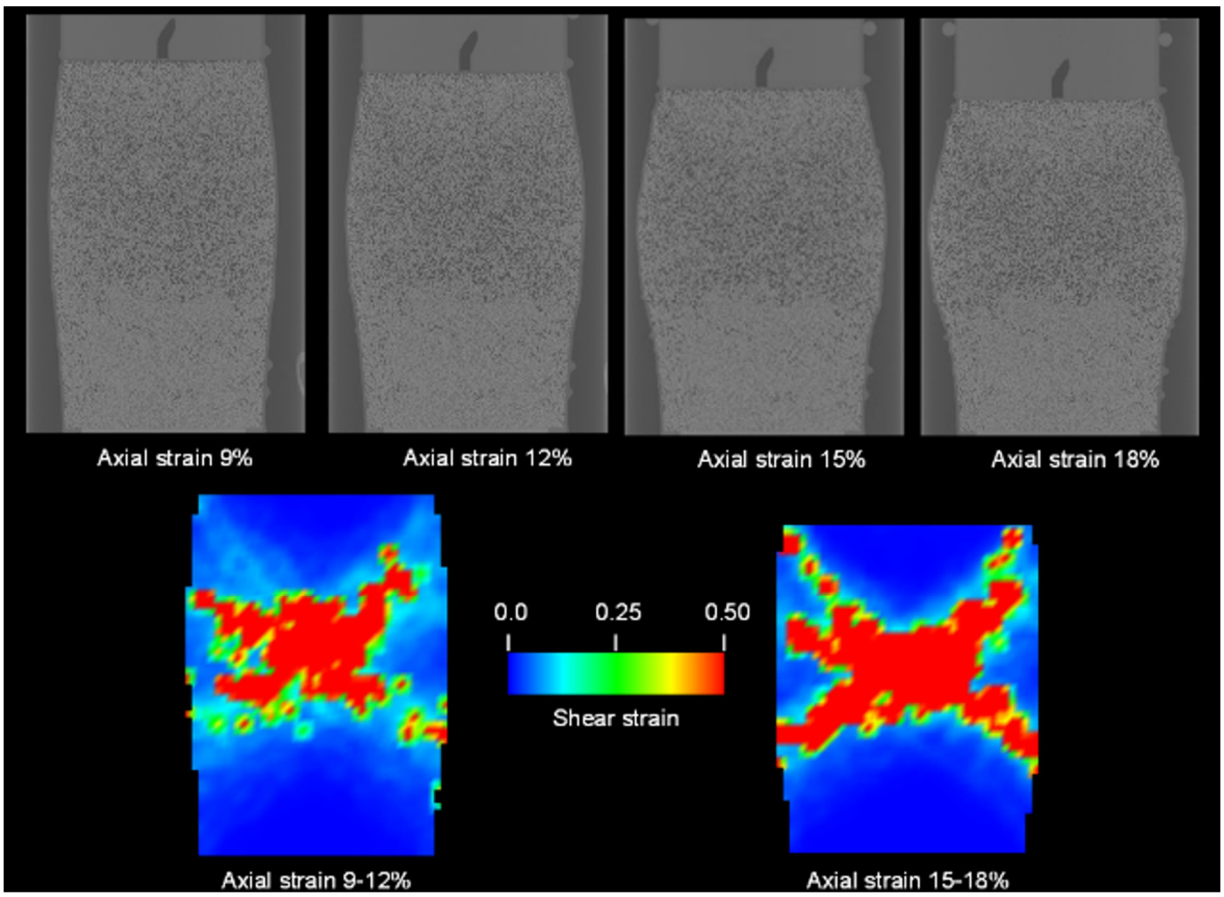

Figure 7. CT images and spatial distribution of shear strain calculated by DIC.

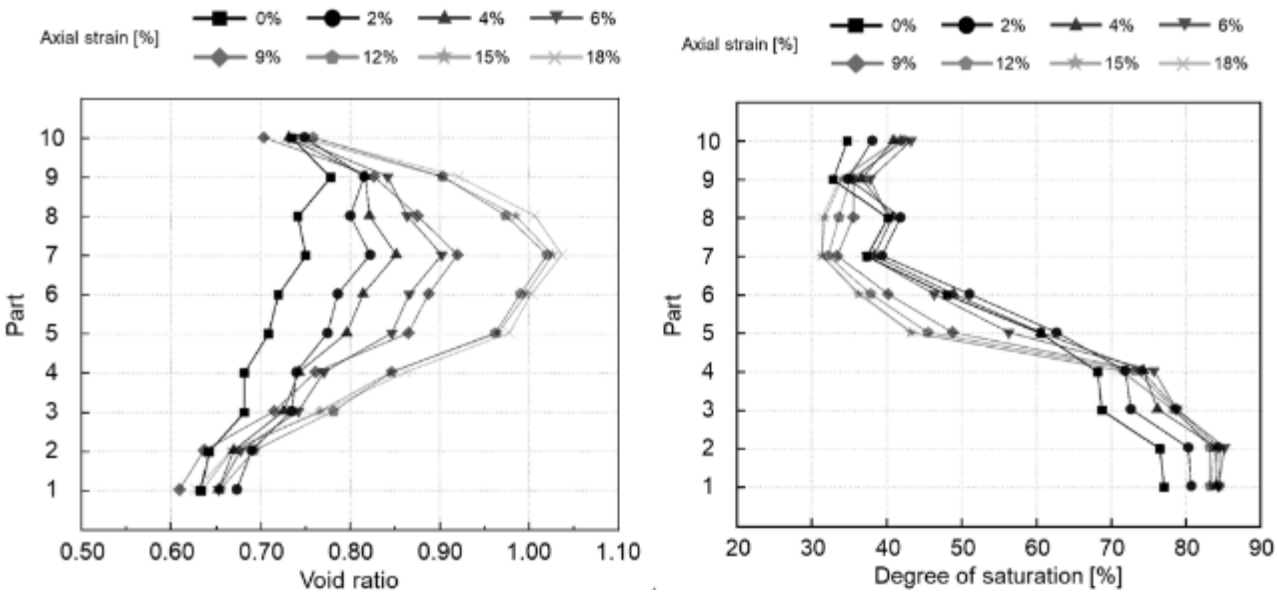

Figure 8. Distributions of void ratio and degree of saturation in the vertical direction of the specimen.

3.2 *Vertical distribution changes in void ratio and degree of saturation*

Figure 8 shows the changes in the distributions of void ratio and degree of saturation in the vertical direction of the specimen. At each axial strain level, the entire segmented image was divided into ten parts along the vertical direction, and the average values for each part were calculated. At 0% axial strain, the void ratio decreases toward the bottom of the specimen. This is likely due to the greater vibration received by the lower layers of sand during the compaction process, as well as the additional compaction from the weight of the upper layers. The degree of saturation is higher at the bottom of the specimen at 0% axial strain. This is because, in the suction method based on water head difference, higher suction is applied to the upper part of the specimen, resulting in relatively more drainage from the top. At 4% axial strain, an increase in void ratio is observed mainly in the upper-middle region of the specimen (parts 6 to 8).

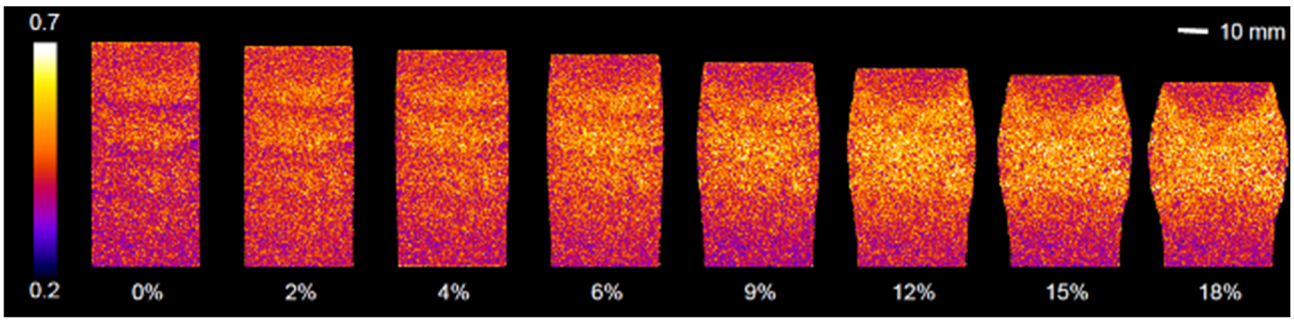

Figure 9. Spatial distribution of porosity in specimen

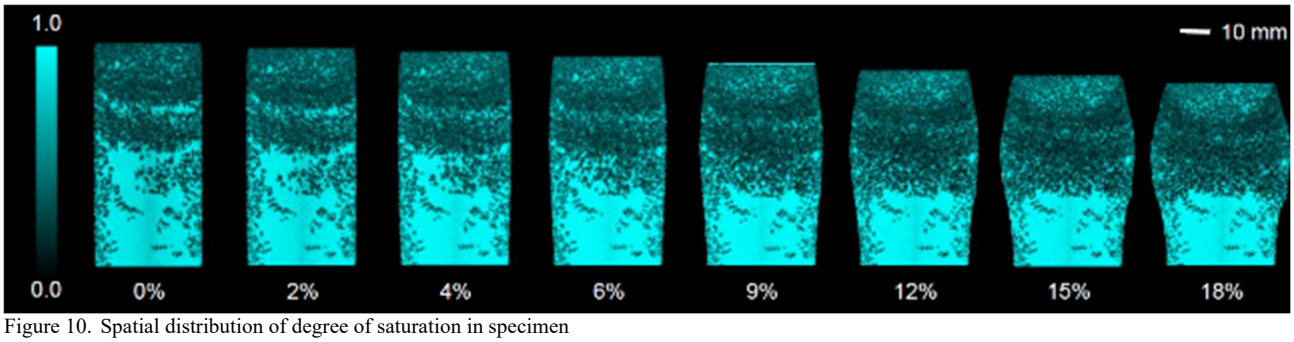

Figure 10. Spatial distribution of degree of saturation in specimen

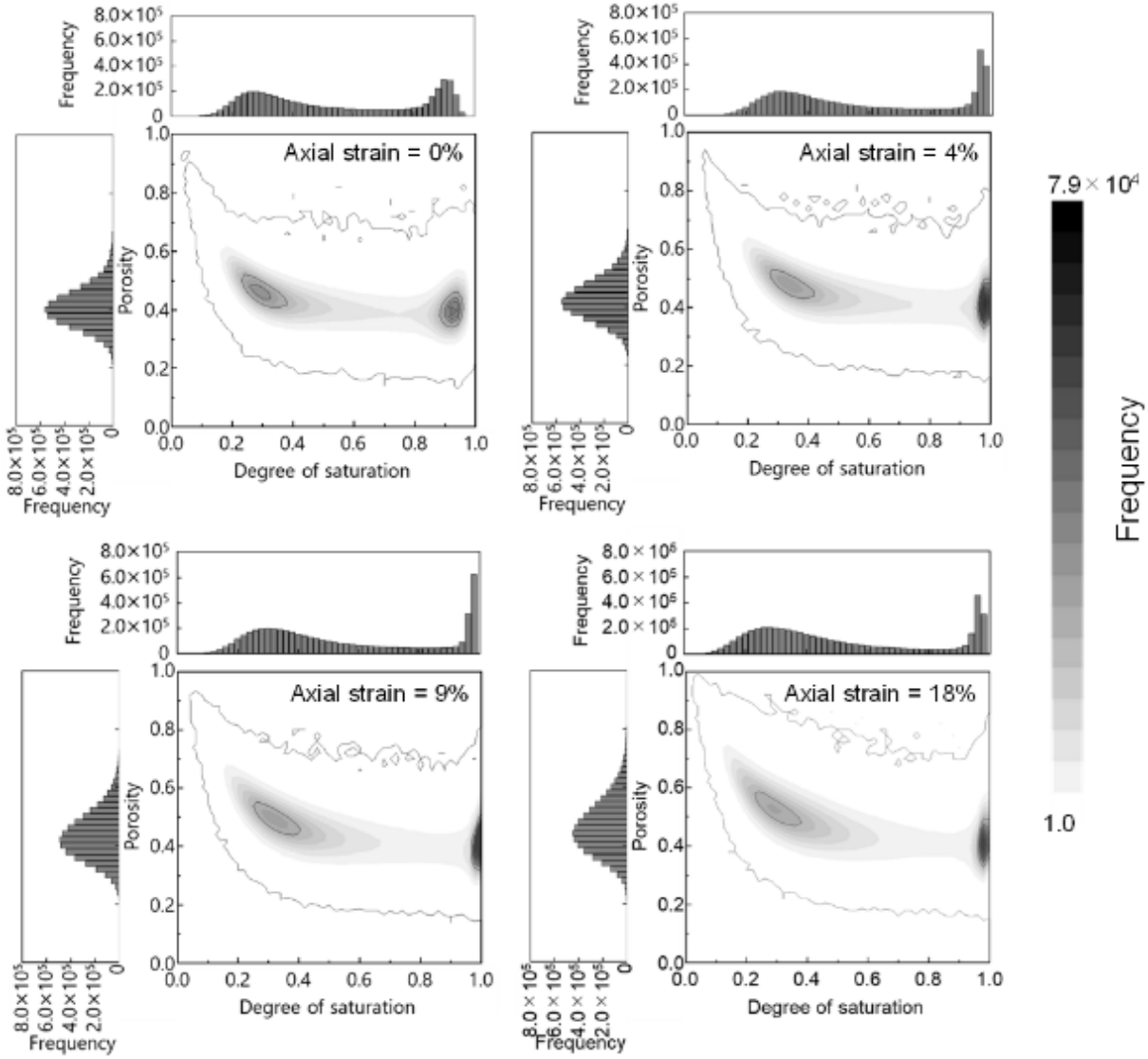

Figure 11. Porosity-degree of saturation relationships at different axial strains

At 9% axial strain, the void ratio increases significantly in Parts 5 to 8, accompanied by a noticeable decrease in degree of saturation. This trend becomes more pronounced after 12% axial strain. In contrast, Parts 1 and 2 at the top and Part 10 at the bottom of the specimen show little change in void ratio from 0% to 18% axial strain, maintaining a dense state, while the degree of saturation in these areas shows a slight increasing trend.

Figures 9 and 10 show the spatial distributions of local porosity and degree of saturation within the specimen, obtained using the cubic subset method. As axial strain increases, regions with high porosity expand around the center of the specimen and extend diagonally from the center. Considering the shear strain distribution shown in Figure 7 and the trend in void ratio changes shown in Figure 8, this can be interpreted as an increase in low-density regions caused by volumetric expansion associated with the development of the shear band. Moreover, regions of increased porosity correspond to regions of decreased degree of saturation, indicating a clear tendency for water retention capacity to decrease with shear band development. In contrast, cone-shaped zones appear at the top and bottom of the specimen, where changes in porosity are minimal. According to the shear strain distribution in Figure 7, these regions experience no plastic deformation and thus can be considered as parts of the specimen outside the shear band that retain a dense particle structure. Therefore, the slight increase in saturation observed in the upper and lower parts of the specimen can be attributed to characteristics of the regions outside the shear band.

Figure 11 presents histograms showing the relationship between porosity and degree of saturation at axial strains of 0%, 4%, 9% and 18%. The data are clustered into two main regions. As axial strain increases, the clusters tend to shift—one toward the lower right (low porosity and high saturation) and the other toward the upper left (high porosity and low saturation). Considering that the triaxial compression test was conducted under undrained conditions, and that water retention capacity decreases within the shear band, it can be interpreted that pore water originally present in the shear band migrated to the surrounding area, where retention capacity is higher.

4 CONCLUSIONS

The authors successfully achieved particle-scale full-field imaging of a triaxial specimen using the high-energy X-ray CT beamline BL28B2 at SPring-8. Specifically, high-resolution images capturing three-phase microstructural changes were obtained throughout the entire partially saturated triaxial specimen, which had a diameter of 35 mm and a height of 71 mm. Image analysis revealed that both density and degree of saturation decreased in the central region of the specimen, whereas the upper and lower regions showed little change in density and a tendency for saturation to increase. Furthermore, under drained conditions for pore air and undrained conditions for pore water, a significant decrease in density and water retention was observed within the shear band. It was also clarified that pore water originally present within the shear band migrated to surrounding regions with higher water retention capacity.

Using the CT images obtained in the present study, further investigations into individual particle kinematics and variations in the microscopic characteristics of pore water—such as pore water morphology, spatial distribution of liquid bridges, curvature of the air–water interface, and so on—are crucial for clarifying the micro–macro relationships in partially saturated soils. To this end, the application of high-performance computing or supercomputers is required to process the very large datasets involved.

5 ACKNOWLEDGEMENTS

We would like to express our sincere gratitude to Kentaro Uesugi and Masato Hoshino for their invaluable support during the experiments conducted at SPring-8. We also wish to thank Kouta Toda for his assistance in organizing the experimental data. This research was financially supported by the Maeda Engineering Foundation in 2024.

6 REFERENCES

Cui, Y.J., and Delage, P. 1996. Yielding and plastic behavior of an unsaturated compacted silt. *Géotechnique* 46(2), 291-311.

Cunningham, M.R., Ridley, A.M., Dineen, K., and Burland, J.B. 2003. The mechanical behavior of a reconstituted unsaturated silty clay. *Géotechnique* 53(2), 183-194.

Higo, Y., Oka, F., Kimoto, S., Sanagawa, T., and Matsushima, Y. 2011. Study of strain localization and microstructural changes in partially saturated sand during triaxial tests using microfocus X-ray CT. *Soils and Foundations* 51(1), 95-111.

Higo, Y., Oka, F., Sato, T., Matsushima, Y., and Kimoto, S. 2013. Investigation of localized deformation in partially saturated sand under triaxial compression using microfocus X-ray CT with digital image correlation. *Soils and Foundations* 53(2), 181-198.

Higo, Y., and Kido, R. 2024. A microscopic interpretation of hysteresis in the water retention curve of sand. *Géotechnique*, 1-9.

Higo, Y., Kido, R., Takamura, F., and Fukushima, Y. 2018. Pore-scale investigations of partially water-saturated granular soil. *Mechanics Research Communications* 94, 1-7.

Hoshino, M., and Uesugi, K. 2023. High-resolution X-ray microtomography at 200 keV region. *Proc. of the 15th International Conference on X-ray Microscopy* (040016), 1-5.

Hoshino, M., Uesugi, K., Shikaku, R., and Yagi, N. 2017. High-energy, high-resolution x-ray imaging for metallic cultural heritages. *AIP Advances* 7(105122), 1-8.

Hoshino, M., Uesugi, K., and Yagi, N. 2020. Development of an X-ray imaging detector for high-energy X-ray microtomography. *Synchrotron Radiation* 27, 934-940.

Kido, R. 2019. Microscopic Characteristics of Partially Saturated Soil and their Link to Macroscopic Responses. *Doctor Dissertation in Kyoto University*.

Kido, R., and Higo, Y. 2020. Microscopic characteristics of partially saturated dense sand and their link to macroscopic responses under triaxial compression conditions. *Acta Geotechnica* 15, 3055-3073.

Kimoto, S., Oka, F., Fukutani, J., Yabuki, T., Nakashima, K. 2011. Monotonic and cyclic behavior of unsaturated sandy soil under drained and fully undrained conditions. *Soils and Foundations* 51(4), 663-681.

Rahardjo, H., Lim, T.T., Chang, M.F., and Fredlund, D.G. 1995. Shear-strength characteristics of a residual soil. *Canadian Geotechnical Journal* 32, 60-77.

Thu, T.M., Rahardjo, H., and Leong, E.C. 2006. Shear strength and pore-water pressure characteristics during constant water content triaxial tests. *Journal of Geotechnical and Geoenvironmental Engineering* 132(3), 411-419.

Wang, J.P., Andò, E., Charrier, P., Salager, S., Lambert, P., Francois, B. 2019. Micro-scale investigation of unsaturated sand in mini-triaxial shearing using X-ray CT. *Géotechnique Letters*, 9, 1-9.